A Second-order Hybrid Finite Element/Volume Method for Viscoelastic Flows

P. Wapperom and M.F. Webster

Institute of Non-Newtonian Fluid Mechanics
Department of Computer Science
University of Wales, Swansea
Singleton Park, Swansea SA2 8PP, UK

Abstract

A second-order accurate cell-vertex finite volume/finite element hybrid scheme is proposed. A finite volume method is used for the hyperbolic stress equations and a finite element method for the balance equations. The finite volume implementation incorporates the recent advancement on fluctuation distribution schemes for advection equations. Accuracy results are presented for a pure convection problem, for which fluctuation distribution has been developed, and an Oldroyd-B benchmark problem. When source terms are included consistently, second-order accuracy can be achieved. However, a loss of accuracy is observed for both benchmark problems, when the flow near a boundary is (almost) parallel to it. Accuracy can be recovered in an elegant manner by taking advantage of the quadratic representations on the parent finite element mesh. Compared to the finite element method, the second-order accurate finite volume implementation is ten times as efficient.

Keywords: Hybrid finite element/finite volume, fluctuation distribution, second-order, Oldroyd-B, pure convection.

1 Introduction

This study investigates the application of a new hybrid scheme to the numerical solution of model and viscoelastic flows. This time-stepping scheme combines both finite element (FE) and finite volume (FV) spatial discretisations. Specific attention is focused on the performance characteristics of such a hybrid method, in terms of accuracy and efficiency, with comparison against a finite element alternative, previously developed for highly elastic flows [1], [2], [3].

There are a number of key features to this work that are novel in the viscoelastic context. First, there is the particular choice of hybrid FE/FV construction. A cell-vertex FV approach is adopted, inspired by the recent work of Morton and co-workers [4], [5], Struijs *et al.* [6] and Tomaich and Roe [7]. This extends their findings for advection, Euler and compressible Navier–Stokes equations into incompressible viscoelastic flows of mixed parabolic/hyperbolic type, containing solution dependent source terms. The method is applied on triangular FE meshes with FV sub-cells, reminiscent of the sub-element FE implementation of Marchal and Crochet [8], though that work was on rectangular meshes. The triangular FV approach has been adopted by Struijs *et al.* [6] and Tomaich and Roe [7] in the cell-vertex form and by Berzins and Ware [9] in the cell-centred case. The cell-vertex instance leads naturally to fluctuation distribution to associate cell contributions with nodal equations, that encompasses properties such as positivity, upwinding and linearity preservation. In contrast, to achieve the same ends, the cell-centred form requires approximate Riemann Solvers and non-linear flux limiters. Compared to cell-centred methods, cell-vertex schemes maintain their accuracy for broader families of non-uniform and distorted meshes, and are less susceptible to spurious modes than their cell-centred counterparts, [10], [4].

Galerkin finite element methods are optimal for self-adjoint problems, and hence are ideal for discretisation of elliptic operators. In contrast, finite volume technology has advanced considerably over the last decade, in its treatment of equations that may be expressed in conservation form such as pure advection equations, and hence their application to hyperbolic equations of first-order in space and time, see Struijs *et al.* [6]. For incompressible viscoelastic flows, with non-trivial source terms, the question arises as to whether a finite element approach may be better suited to solve for the field equations, concerned with the conservation of mass and momentum (parabolic type), whilst a finite volume approach may be more appropriate for the advection-dominated constitutive law (hyperbolic type). For example, recent work on advection equations with structured and unstructured grids has shown that fluctuation distribution schemes can capture steep gradients accurately, [6].

The literature on finite element methods for viscoelastic flows is broad. Some of the more robust schemes of recent years have shown that it is possible to solve for highly elastic, smooth and non-smooth flows [1], [2]. This has produced algorithms of EVSS [11], space-time/Galerkin Least squares with discontinuous stress [12], DEVSS [13] and DEVSS/DG [14] and Recovery-Taylor–Galerkin types [3]. Nevertheless, the FE approach does carry with it a heavy computational penalty in complex flows, that necessitates sophisticated numerical strategies in dealing with upwinding, accurate representation of velocity gradients and the coupling of the system. This is an important issue to address, specifically as three-dimensional [15], [16] and multi-mode viscoelastic [12], [17] computations are now being undertaken.

It is for this reason that attention has been devoted to alternative techniques, such as that embodied in FV methodology, that require less memory and CPU time than do their FE counterparts. This method arose from the finite difference domain, being extended

to embrace conservation laws stated in integral form on control volumes (see Hirsch [10]). This naturally incorporates the fluxes of the system in a localised manner, as integrals on boundaries of control volumes, with source terms taken as associated area integrals, and is ideal for hyperbolic systems. The location of variables and juxtaposition with respect to control volume impact upon the equations constructed. The cell-centred choice may be equivalenced to a piecewise constant solution interpolation, whilst correspondingly a cell-vertex form equates to linear interpolation. In this respect, the commonly employed staggered grid system is an overlapping arrangement, that essentially mimics the cell-centred approach.

Experiences with FV methods for viscoelastic flow fall into two categories, those with a complete FV implementation and those of a hybrid form. The most common class is the former, invoking a full FV implementation for primitive variables of velocity, pressure and stress, such as documented by Eggleston *et al.* [18], Darwish *et al.* [19] and Tanner and co-workers ([20], [21]). Hybrid approaches have been developed by Sato and Richardson [22] and Yoo and Na [23]. The majority of these studies investigate steady two-dimensional flows, with the exceptions of [16], [24]. To date, most studies have concentrated on establishing the viability of the particular FV implementation, considering in particular stability issues, attempting to achieve high elasticity solutions to benchmark problems (see for example, Sato and Richardson [22], and Yoo and Na [23] for solving the 4:1 contraction flow). Accuracy of schemes has not been given extensive coverage in the viscoelastic domain, and this we attend to here. Most studies adopt a time-stepping solution procedure (bar Darwish *et al.* [19] and Yoo and Na [23]), and consider a staggered grid system to eliminate spurious pressure modes with SIMPLER-type algorithms to search for a steady solution. Rectangular grids are taken by most (normally implying with structure) and there are no other cell-vertex studies to our knowledge.

Most pertinent of those references cited above are the two sources, Sato and Richardson and Tanner and co-workers. The hybrid FE/FV study of Sato and Richardson is one that employs a time-explicit FE method for momentum and FV for pressure and stress. A cell-centred FV scheme is solved implicitly in time for stress. This implementation uses a TVD (Total Variation Diminishing [10]) flux-corrected transport scheme applied to the advection terms of the constitutive equation, essentially a form of higher-order upwinding. The present study contrasts to this work via retaining an FE treatment of the pressure, and the alternative FV choices for stress outlined above. The articles by Tanner and co-workers ([20], [21]), prove of interest due to the artificial diffusion incorporated on both sides of the constitutive equation. This is a convergence stabilisation strategy, rather similar in style to the SU (Streamline Upwind) method of Marchal and Crochet [8].

The finite element framework, upon which this hybrid algorithm is grafted, is a semi-implicit time-stepping Taylor–Galerkin/pressure-correction scheme of fractional stages. The FE treatment of the constitutive equation incorporates consistent Petrov–Galerkin streamline upwinding (SUPG) and recovery for velocity gradients. In two dimensions, the finite element grid is constructed as a triangular tessellation, with pressure nodes located at the vertices and velocity/stress components at both vertices and mid-side nodes. In the FE/FV hybrid scheme, a cell vertex approach is adopted in the FV part for the constitutive equation. A two-step Lax–Wendroff time-stepping is built into this scheme, as with the FE scheme above, that is a popular choice of iterative smoother [5]. There is a natural complementarity to the structure of the scheme, as one switches between the two choices of FE or FV discretisation for stress. Four linear FV triangular cells are constructed as subcells of each

parent quadratic FE triangular cell, by connecting the mid-side nodes. With stress variables located at the vertices of the FV cells, no interpolation is required to recover the FE nodal stress values.

A Cartesian benchmark flow problem is proposed in our investigation that displays analytical solutions. This problem is two-dimensional in nature and may be stated in pure convection form, or in the presence of source terms for an Oldroyd-B model. As such, this problem may be solved for multiple scalar components by varying the boundary conditions, each component being decoupled from the others. Such a problem has been developed to reflect greater complexity than the sink flow discussed in [25], which in contrast is one-dimensional. The possibility arises of investigating situations with different inflow side numbers, that is all important to distinguish between the merits of various fluctuation distribution schemes. Both circumstances of frozen kinematics and coupled stress/kinematics are addressed in this manner. Orders of accuracy and efficiency in attaining solutions are established.

2 Governing equations

For incompressible and isothermal flow, the balance of mass and linear momentum in non-dimensional form are:

$$\nabla \cdot \boldsymbol{u} = 0, \tag{1}$$

$$Re\frac{\partial \boldsymbol{u}}{\partial t} = -Re\ \boldsymbol{u}\cdot\nabla\boldsymbol{u} - \nabla p + \nabla\cdot\left(2\frac{\mu_{\rm s}}{\mu}\boldsymbol{d} + \boldsymbol{\tau}\right), \tag{2}$$

where $\boldsymbol{u}$ is the fluid velocity, p the hydrodynamic pressure, $\boldsymbol{I}$ the unit tensor, $\boldsymbol{\tau}$ the extra-stress tensor, $\mu_{\rm s}$ the solvent viscosity and the Euler rate-of-deformation tensor $\boldsymbol{d} = (\boldsymbol{L} + \boldsymbol{L}^T)/2$, with $\boldsymbol{L}^T = \nabla\boldsymbol{u}$ the velocity gradient.

To establish the theory, we adopt the Oldroyd-B model to represent the stress. Extension to more complex models, such as Phan-Thien–Tanner, Giesekus or FENE (see for example [26]), is straightforward. The constitutive equation for the Oldroyd-B model is given by:

$$We\frac{\partial \boldsymbol{\tau}}{\partial t} = -We\ \boldsymbol{u}\cdot\nabla\boldsymbol{\tau} + We\,(\boldsymbol{L}\cdot\boldsymbol{\tau} + \boldsymbol{\tau}\cdot\boldsymbol{L}^T) + 2\frac{\mu_{\rm e}}{\mu}\boldsymbol{d} - \boldsymbol{\tau}, \tag{3}$$

where $\mu_{\rm e}$ is the elastic viscosity and the total viscosity is $\mu = \mu_{\rm e} + \mu_{\rm s}$. When $\mu_{\rm s} = 0$ we have the Maxwell model. Non-dimensional numbers of relevance here are the Reynolds and the Weissenberg number, defined as

$$Re = \frac{\rho U L}{\mu}, \qquad\qquad We = \frac{\lambda U}{L}, \tag{4}$$

where ρ is the fluid density, λ the fluid relaxation time, U a characteristic velocity and L a characteristic length scale of the flow.

3 Numerical method

To search for the steady-state solution, a Lax–Wendroff time-stepping scheme is employed based on a Taylor series expansion in time. To obtain an $\mathcal{O}(\Delta t^2)$ accurate scheme, that avoids the explicit evaluation of the Jacobian, a two-step approach is chosen and to handle the incompressibility constraint, we use a pressure-correction method, see [27], [28]. The

resulting solution method may be stated in general form, irrespective of the discretisation method, consisting of three stages. At stage 1, where the two-step predictor-corrector is embedded, the momentum and stress equations are solved:

$$\begin{aligned} A_u(\mathcal{U}^{n+1/2} - \mathcal{U}^n) &= \frac{\Delta t}{2Re} b_u(\mathcal{P}^n, \mathcal{U}^n, \mathcal{T}^n), \\ A_\tau(\mathcal{T}^{n+1/2} - \mathcal{T}^n) &= \frac{\Delta t}{2\,We} b_\tau(\mathcal{U}^n, \mathcal{T}^n), \\ A_u(\mathcal{U}^* - \mathcal{U}^n) &= \frac{\Delta t}{Re} b_u(\mathcal{P}^n, \mathcal{U}^n, \mathcal{U}^{n+1/2}, \mathcal{T}^{n+1/2}), \\ A_\tau(\mathcal{T}^{n+1} - \mathcal{T}^n) &= \frac{\Delta t}{We} b_\tau(\mathcal{U}^{n+1/2}, \mathcal{T}^{n+1/2}), \end{aligned} \tag{5}$$

where $\mathcal{U}$, $\mathcal{T}$ and $\mathcal{P}$ are vectors of nodal point values of the discretised velocity, extra stress and pressure. The velocity and extra stress are approximated by quadratic functions per finite element, using vertices and mid-side nodes. The pressure is approximated by a linear function using the vertices alone.

The momentum equations are discretised with the Galerkin finite element method. The diffusive terms are treated in a semi-implicit manner to enhance stability, as discussed in [28]. The resulting matrix-vector equation for the momentum equation is solved with a Jacobi iterative method, using no more than five iterative sweeps [28]. When we use a finite volume method, the matrix A_τ is the identity matrix, while for a finite element method it is a sparse matrix. The resulting matrix-vector equation is solved similarly as for the momentum equation. The vector b_τ represents the discretisation of the right-hand side of Eq. (3), its precise form depending on the FV or FE discretisation. Using the hybrid FE/FV, thus, avoids the need to solve a matrix-vector equation for the extra stress, and the right-hand side b_τ is easier to construct. This is advantageous from an efficiency viewpoint, particularly for 3D or multi-mode computations. The details of the finite volume discretisation are outlined below in sections 4 and 5.

To benchmark the hybrid finite element/finite volume scheme we compare its performance against a pure finite element Taylor–Galerkin/pressure-correction method, with SUPG for the stress equations, see [1], termed FE/SUPG. The SUPG upwind test function is given by

$$\boldsymbol{\phi}_{\mathrm{u}} = \boldsymbol{\phi}_{\mathrm{g}} + \alpha_{\mathrm{u}} \boldsymbol{u} \cdot \nabla \boldsymbol{\phi}_{\mathrm{g}}, \tag{6}$$

where $\boldsymbol{\phi}_{\mathrm{g}}$ is the quadratic Galerkin test function. The upwind parameter α_{u} follows the definition

$$\alpha_{\mathrm{u}} = \begin{cases} g^{-1/2} & g \geq 1 \\ g^{1/2} \Delta t^2 & g < 1 \end{cases}, \tag{7}$$

with

$$g = \sum_{l=1}^{3} (\boldsymbol{u} \cdot \nabla \xi_l)^2, \tag{8}$$

where ξ_l are the barycentric coordinate functions on a finite element, following the classical definitions given in [1].

The second-order implementation of pressure correction requires the temporal incrementation of pressure (in a weak form Poisson equation) and velocity. In stage 2, the pressure

at the next time step $(n+1)$ is calculated, and in stage 3, incompressibility is enforced:

$$A_2(\mathcal{P}^{n+1} - \mathcal{P}^n) = b_2(\mathcal{U}^*), \tag{9}$$

$$A_3(\mathcal{U}^{n+1} - \mathcal{U}^*) = b_3(\mathcal{P}^n, \mathcal{P}^{n+1}), \tag{10}$$

where homogeneous Neumann boundary conditions on the temporal increment of pressure are used and for $\mathcal{U}^*$ the same boundary conditions are applied as to $\mathcal{U}^{n+1}$, see detailed discussion in [27], [28]. The pressure is fixed at one point to eliminate the undetermined integration constant. For reasons of accuracy, Eq. (9) is solved by a direct solution method, using Choleski decomposition, whilst Eq. (10) is solved iteratively as above.

The truncation criteria we have employed for the time stepping procedure are

$$\begin{aligned} \frac{Re}{\Delta t}\frac{||\mathcal{U}^{n+1} - \mathcal{U}^n||_2}{||\mathcal{U}^{n+1}||_2} &\leq \epsilon, \\ \frac{||\mathcal{P}^{n+1} - \mathcal{P}^n||_2}{||\mathcal{P}^{n+1}||_2} &\leq \epsilon, \\ \frac{We}{\Delta t}\frac{||\mathcal{T}^{n+1} - \mathcal{T}^n||_2}{||\mathcal{T}^{n+1}||_2} &\leq \epsilon, \end{aligned} \tag{11}$$

where ϵ is a small parameter, normally taken as 10^{-8}.

4 Flux (fluctuation) distribution schemes

Recently, fluctuation distribution has been introduced in [6], using triangular meshes with a cell-vertex finite volume method. Originally, the method was developed for pure convection problems with a constant advection speed $\boldsymbol{a}$:

$$\frac{\partial \phi}{\partial t} = -\boldsymbol{a} \cdot \nabla \phi, \tag{12}$$

where ϕ is some scalar quantity. Fluctuation distribution (FD) is the term used to describe the non-uniform distribution of the fluctuation of a finite volume cell to its member nodes. The fluctuation is a local flux imbalance causing a non-zero time derivative of the local solution. In our extension to the method, sources are present as well (see section 5), so the flux term does not vanish in equilibrium. Hence 'flux distribution' is a more appropriate term to describe the present implementation.

Integration over a finite volume subcell T yields

$$\int_T \frac{\partial \phi}{\partial t}\, \mathrm{d}\Omega_T = \oint_{\Gamma_T} \phi \boldsymbol{a} \cdot \boldsymbol{n}\, \mathrm{d}\Gamma_T \equiv \oint_{\Gamma_T} \boldsymbol{R} \cdot \boldsymbol{n}\, \mathrm{d}\Gamma_T \equiv R_T, \tag{13}$$

where $\boldsymbol{n}$ is the *inward* normal, $\boldsymbol{R}$ the flux vector and R_T is the resultant flux over triangle T.

For linear ϕ and constant $\boldsymbol{a}$ the line integral in Eq. (13) is evaluated exactly with the trapezoidal rule. For the flux over triangle T, we obtain

$$R_T = -\sum_{l=1}^{3} k_l \phi_l, \tag{14}$$

where the coefficients k_l are

$$k_l = \frac{1}{2}\boldsymbol{a} \cdot \boldsymbol{n}_l, \tag{15}$$

and $\boldsymbol{n}_l$ represents the *inward* normal to the cell on the side opposite vertex l, scaled to be of equal length to the side with which it is orthogonal, so that $\sum_l \boldsymbol{n}_l = 0$. Additionally, due to the constant advection velocity $\boldsymbol{a}$, we have

$$\sum_{l=1}^{3} k_l = 0. \tag{16}$$

Within the FD scheme, the flux R_T is calculated over the individual finite volume cells T and then distributed to the nodes of that cell. The update from triangle T to vertex l on that triangle is

$$\hat{\Omega}_l \frac{\phi_l^{n+1} - \phi_l^n}{\Delta t} = \alpha_l^T R_T, \tag{17}$$

where $\hat{\Omega}_l$ is the area associated with node l. We will return to this in section 5. The coefficients α_l^T are weights which determine the *distribution of the flux* R_T to vertex l of triangle T.

The criteria for the suitable choice of α_l^T are

a) *conservation:*

Conservation yields the requirement that the sum of the coefficients α_l over the vertices l of each triangle T equals:

$$\sum_l \alpha_l^T = 1. \tag{18}$$

b) *positivity:*

Positivity means that ϕ_l^{n+1} is a convex combination of nodal values at the previous time step, ϕ_j^n:

$$\phi_l^{n+1} = \sum_j c_j \phi_j^n, \tag{19}$$

where the coefficients c_j are positive. Positivity guarantees a maximum principle for the discrete steady state solution of the linear advection equation, thus prohibiting the occurrence of new extrema and imposing stability on the explicit scheme [6]. A stronger, but more easily verifiable condition, is local positivity, which requires that the contribution of each triangle, taken separately, is positive. A linear positive scheme is TVD. For nonlinear schemes, the positivity criterion is less stringent than TVD, whilst still maintaining the favourable properties of suppression of new extrema in the solution and guaranteeing *stability* of the explicit time-stepping scheme. Ensuring positivity of the flux distribution has been only an issue for the flux terms and may not be an appropriate criterium for source term treatment; the presence of sources may produce new, physically meaningful extrema that should not be suppressed.

c) *linearity preservation:*

Linearity preservation requires that the scheme maintains the steady state solution exactly, whenever this is a linear function in space for an arbitrary triangulation of the domain. This is closely related to the notion of *second order accuracy*, commonly discussed under finite difference schemes, although it is an accuracy requirement on the spatial discretisation only.

A linear scheme does not have to be linearity preserving. For a linear scheme, ϕ_l^{n+1} is a linear combination of solution values at the previous time step n, so that the coefficients c_j in Eq. (19) are constant.

When written in the form (17), the two possibilities of having a linear scheme, are either for the coefficients α_l^T to be independent of ϕ, in which case it is linearity preserving, or for

$$\alpha_l^T = \frac{\beta_l^T}{R_T}, \tag{20}$$

where the coefficients β_l^T depend linearly on ϕ summing to R_T. This fact can be used to prove that linear schemes cannot be both positive and linearity preserving [6]. If one uses the coefficients β_l^T to express the distribution, instead of the coefficients α_l^T, then Eq. (17) becomes

$$\hat{\Omega}_l \frac{\phi_l^{n+1} - \phi_l^n}{\Delta t} = \beta_l^T. \tag{21}$$

For certain flux distribution schemes, notably linear positive schemes, it is more convenient to express the distribution in terms of the coefficients β_l^T.

At this point, it is convenient to divide linear schemes into two classes, those that satisfy positivity and the remainder that satisfy linearity preservation. Only a *nonlinear* scheme can satisfy both of these properties simultaneously.

4.1 Choices for α_l and β_l

In this section, we discuss some choices for the coefficients α_l^T in Eq. (17) and β_l^T in Eq. (21). Henceforth, we drop the superscript ^{T} in the α and β coefficients, for reasons of clarity. We first note that a standard finite volume approach is recovered when a uniform distribution is chosen, that is $\alpha_i = \alpha_j = \alpha_k = 1/3$, where $\{i, j, k\}$ denotes the vertices of the FV-cell.

For FD-schemes, distinction is made on triangles with one and two inflow sides. Both situations are illustrated in Figs. 1 and 2. The inflow sides are determined by the sign of the coefficients k_l - a positive k_l indicates that the constant advection speed $\boldsymbol{a}$ is inflowing into the side opposite vertex l. Due to Eq. (16), it is ensured that each triangle has a maximum of two inflow sides and a maximum of two outflow sides.

Triangular cells, having only one inflow side, can satisfy the positivity and linearity preservation properties by sending the whole flux to the downstream node, see [6]. In the case with $k_i > 0$, $k_j < 0$, $k_k < 0$, see Fig. 1, we would have

$$\alpha_i = 1, \qquad \alpha_j = 0, \qquad \alpha_k = 0. \tag{22}$$

The various FD-schemes only differ for the case of two inflow sides. We will briefly discuss some of the FD-schemes below: one satisfying positivity, one satisfying linearity preservation and one satisfying both (a nonlinear variant). An extensive description of these and other FD-schemes is provided in [6].

4.1.1 N-scheme

The N-scheme, or Narrow-scheme, is a linear β-scheme that is positive. It is optimal in the sense that it uses the maximum allowable time-step and the most narrow stencil. The resulting β-coefficients of the N-scheme, for the case of two inflow sides as illustrated in Fig. 2, are

$$\begin{aligned} \beta_i &= -k_i(\phi_i - \phi_k), \\ \beta_j &= -k_j(\phi_j - \phi_k), \\ \beta_k &= 0. \end{aligned} \tag{23}$$

where coefficients k follow from Eq. (15).

4.1.2 Low Diffusion B scheme

The Low Diffusion B (LDB) scheme is a linear α-scheme that is linearity preserving. It shows a relatively small amount of numerical diffusion in comparison with a linear positive scheme. The LDB-scheme is based on the angles in the triangle on both sides of the advection speed $\boldsymbol{a}$. The alternative LDA-scheme is based on the corresponding area split of the triangle. The coefficients α_l in Eq. (17) are

$$\begin{aligned} \alpha_i &= (\sin\gamma_1 \cos\gamma_2)/\sin(\gamma_1+\gamma_2), \\ \alpha_j &= (\sin\gamma_2 \cos\gamma_1)/\sin(\gamma_1+\gamma_2), \\ \alpha_k &= 0, \end{aligned} \tag{24}$$

where the angles γ_1 and γ_2 are defined in Fig. 3. The closer advection speed $\boldsymbol{a}$ is to being parallel to one of the boundary sides, the larger is the contribution to the downstream node at that boundary.

4.1.3 PSI-scheme

The PSI-scheme is a non-linear scheme that is both positive and linearity preserving. It is equivalent to the N-scheme with a MinMod limiter [6]. This may be interpreted as an α-scheme, with the aid of Eq. (20) and safeguard for vanishing R_T. If we denote the β-coefficients of the PSI-scheme by β_l^* and of the N-scheme by β_l, as in Eq. (23), we have

$$\begin{aligned} \beta_i^* &= \beta_i - L(\beta_i, -\beta_j), \\ \beta_j^* &= \beta_j - L(\beta_j, -\beta_i), \end{aligned} \tag{25}$$

where L is the MinMod limiter function defined by

$$L(x,y) = \frac{1}{4}(1+\mathrm{sign}(xy))(\mathrm{sign}(x)+\mathrm{sign}(y))\,\min(|x|,|y|), \tag{26}$$

where the sign operator for argument x is given by

$$\mathrm{sign}(x) = \begin{cases} -1 & \text{if } x<0 \\ 0 & \text{if } x=0 \\ 1 & \text{if } x>0. \end{cases} \tag{27}$$

The scheme only deviates from the N-scheme if $\beta_i\beta_j < 0$.

4.2 Extension to nonlinear advection equations

In the case of a non-constant advection speed $\boldsymbol{u}$, we have

$$\frac{\partial\phi}{\partial t} = -\boldsymbol{u}\cdot\nabla\phi. \tag{28}$$

Extension to the above theory with departure from a constant advection speed $\boldsymbol{a}$, consists in finding a conservative linearised advection speed $\overline{\boldsymbol{a}}$, as described in [6], that satisfies

$$\int_\Omega \boldsymbol{u}\cdot\nabla\phi \,\mathrm{d}\Omega = \int_\Omega \overline{\boldsymbol{a}}\cdot\nabla\phi \,\mathrm{d}\Omega. \tag{29}$$

Due to the linearity of ϕ (constant gradient), then

$$\overline{\boldsymbol{a}} = \frac{1}{\hat{\Omega}}\int_\Omega \boldsymbol{u}\,\mathrm{d}\Omega. \tag{30}$$

Hence, in discretised form on a FV triangle T, we gather

$$\overline{\boldsymbol{a}} = \frac{1}{3}\sum_{l=1}^{3} \boldsymbol{u}_l, \tag{31}$$

the average value of the velocity on the triangle, equating to the centroid value for a linear interpolant. The flux R_T, given by Eq. (13), in terms of the linearised advection speed becomes

$$R_T = \oint_{\Gamma_T} \phi \overline{\boldsymbol{a}} \cdot \boldsymbol{n} \, \mathrm{d}\Gamma_T. \tag{32}$$

Due to the constant advection speed, the trapezoidal rule is sufficient to evaluate the flux R_T exactly, along the finite volume boundaries. So for the coefficients k_l we now have

$$k_l = \frac{1}{2}\overline{\boldsymbol{a}} \cdot \boldsymbol{n}_l. \tag{33}$$

Note that using the (constant) linearised advection speed ensures a maximum of two inflow and outflow sides on a FV triangle.

5 The hybrid Finite Element/Finite Volume Method

The finite element mesh used consists of triangles equipped with quadratic functions for the velocity and stress, and linear functions for the pressure. The velocity and stress are located at the vertices and mid-side nodes, the pressure at the vertices. To apply the flux distribution schemes described in section 4 directly, we require triangles with only vertices. A cell-vertex finite volume mesh can be constructed by dividing each parent finite element into four finite-volume subcells, as indicated in Fig. 4. For stress, by allotting for linear rather than quadratic elements, one order of accuracy is sacrificed compared to the pure finite element method.

For the FV method, the Maxwellian constitutive equation (3) may be written in conservative form, with recourse to the incompressibility constraint, viz,

$$\frac{\partial \boldsymbol{\tau}}{\partial t} = -\nabla \cdot \mathcal{R} + \boldsymbol{Q}, \tag{34}$$

where the flux $\mathcal{R}$ and the source $\boldsymbol{Q}$ are

$$\mathcal{R} = \boldsymbol{u}\boldsymbol{\tau}, \tag{35}$$

$$\boldsymbol{Q} = \frac{1}{We}(2\frac{\mu_{\mathrm{e}}}{\mu}\boldsymbol{d} - \boldsymbol{\tau}) + \boldsymbol{L}\cdot\boldsymbol{\tau} + \boldsymbol{\tau}\cdot\boldsymbol{L}^T. \tag{36}$$

Note, that when linear (finite volume) representations are employed, $\boldsymbol{L}$ and $\boldsymbol{d}$ reduce to constants per FV-cell. If they are obtained from the quadratic FE representation, they are linear functions.

Each of the stress components can be treated as a scalar function, denoted as ϕ, acting in an arbitrary volume Ω. The variation of the quantity ϕ is controlled through the variation of the flux vector $\boldsymbol{R} = \boldsymbol{u}\phi$ and the scalar source term Q.

Integration of Eq. (34) over a control volume Ω for a scalar stress component ϕ, with the aid of the Gauss divergence theorem on the flux term, yields

$$\frac{\partial}{\partial t}\int_{\Omega} \phi \, \mathrm{d}\Omega = \oint_{\Gamma} \boldsymbol{R}\cdot\boldsymbol{n} \, \mathrm{d}\Gamma + \int_{\Omega} Q \, \mathrm{d}\Omega. \tag{37}$$

The flux integral may be evaluated as discussed in section 4.2. Correspondingly, the source term integral is evaluated from the linear velocity and stress representations per FV-cell. Alternatively, as the FV-mesh is constructed directly from the parent FE-mesh (with quadratic functions), we may still retain the quadratic functions for evaluation of the FV integrals. Obviously, this will demand more computational effort than the linear representation. However, as we proceed to demonstrate in sections 7 and 8, this has important implications with respect to attenuation of optimal levels of accuracy.

In the original method of [6], the integration of the time-derivative term is performed on median dual cells (MDC). For node i the MDC is illustrated in Fig. 5. This zone is constructed around a node on its control volume, by connecting midside positions to triangle centroids, and has area one third of the control volume. As the source terms are of a similar form, it would seem appropriate to treat these in a likewise fashion, by recourse to a MDC approach. However, this approach is found to be inconsistent: there is incompatibility due to the selection of different areas for the source and flux terms. To clarify this issue, we will consider the two finite elements illustrated in Fig. 6 starting from the steady-state solution. The MDC approach always contributes a third of the source integral of both FV cells to node 1 at the bottom left corner. For a one-dimensional flow in the y-direction, the whole flux of triangle 134 is sent to node 1. The contributions are not in equilibrium and this produces considerable update to node 1. Thus, source terms must be treated in a consistent manner, that necessitates the same distribution scheme as used for the convection terms (recall consistent upwinding in FE). As the time-derivative term is similar to the source terms, the argument again holds for that term. This is most probably the reason for the inaccuracy in the time-dependent solutions for pure convection problems reported in [29]. So, with accuracy in mind, the MDC approach may only be used for steady state solutions. For transient problems, the time-derivative term demands a consistent treatment to capture accuracy.

The above deliberations lead to the following modification of Eq. (17) when source terms are present:

$$\hat{\Omega}_l \frac{\phi_l^{n+1} - \phi_l^n}{\Delta t} = \alpha_l^T (R_T + Q_T), \tag{38}$$

where Q_T is the source integral over the control volume of triangle T. Integration of the source terms is performed by an integration rule with appropriate accuracy. For the consistent treatment of the time-derivative term $\hat{\Omega}_l = \alpha_l^T \hat{\Omega}_T$, with $\hat{\Omega}_T$ the area of control volume triangle T. For the MDC approach, $\hat{\Omega}_l$ is equal to the area of the median dual cell around node l in triangle T.

6 Problem description

To test the accuracy of the finite volume method we have developed a two-dimensional Cartesian test problem on a square of unit area. We use a structured, uniform, quadrilateral-based, triangular finite element mesh, as shown in Fig. 7 for the 2x2 mesh. To test for accuracy, we will use similar meshes consisting of 4x4, 8x8 and 16x16 elements, which have mesh size (side) h of 0.5, 0.25, 0.125 and 0.0625, respectively. For the velocity field, illustrated in Fig. 8, we define $u_x = x$ and $u_y = -y$. We consider flow problems for both pure convection and that for the Oldroyd-B model. Boundary conditions for the stress (or ϕ) must be specified on the inflow boundaries $x = x_0$ and $y = y_1$. For Oldroyd-B, the equations are solved for both scenarios of fixed (uncoupled) and calculated velocity field (coupled). For the time-stepping procedure initial conditions are generally taken as quiescent by default. We compute results

for three square domains, that generate varying flows, with different coordinates for the lower and upper boundary: the first, $y_0 = 1$, $y_1 = 2$; the second, $y_0 = 0.1$, $y_1 = 1.1$; and the third, $y_0 = 0$, $y_1 = 1$, referred to as domain 1, 2 and 3, respectively. For all domains the coordinates of the left and right boundary are $x_0 = 1$ and $x_1 = 2$.

6.1 Pure convection problem

First, we consider the pure convection equation for $\boldsymbol{u} = (x, -y)$,

$$\boldsymbol{u} \cdot \nabla\phi = x\frac{\partial\phi}{\partial x} - y\frac{\partial\phi}{\partial y} = 0. \tag{39}$$

Depending upon the specification of boundary conditions, that determine the constants a, b, and c, this equation admits solutions of the form,

$$\phi = a(xy)^c + b. \tag{40}$$

We consider three alternative instances: bilinear ($c = 1$), non-integral power ($c = 1.5$) and biquadratic ($c = 2$), for which we have,

$$\begin{aligned} \phi_1 &= 1 + xy, \\ \phi_2 &= 1 + (xy)^{1.5}, \\ \phi_3 &= 1 + (xy)^2. \end{aligned} \tag{41}$$

Isolines of ϕ_i are aligned with the velocity field. As an example, isolines for ϕ_2 are illustrated in Fig. 9. Isolines for ϕ_1 and ϕ_3 are of identical pattern to those of ϕ_2, differing only in contour levels. On the two inflow boundaries, at $x = x_0$ and $y = y_1$, the corresponding values of ϕ_i are prescribed.

To measure accuracy we use $||\Delta\phi||_\infty$, the maximum norm of the difference from the exact solution scaled by the maximum value of all ϕ_i.

6.2 Oldroyd-B flow problem

For the Oldroyd model, the stress components decouple for the particular linear velocity field in question. The three individual components obey the following equations:

$$\begin{aligned} We(x\frac{\partial\tau_{xx}}{\partial x} - y\frac{\partial\tau_{xx}}{\partial y}) &= 2\frac{\mu_e}{\mu} + (2\,We - 1)\tau_{xx}, \\ We(x\frac{\partial\tau_{xy}}{\partial x} - y\frac{\partial\tau_{xy}}{\partial y}) &= -\tau_{xy}, \\ We(x\frac{\partial\tau_{yy}}{\partial x} - y\frac{\partial\tau_{yy}}{\partial y}) &= -2\frac{\mu_e}{\mu} - (2\,We + 1)\tau_{yy}. \end{aligned} \tag{42}$$

Note, that for this problem, both convection and source terms are important. The three stress components, represented as $(\tau_{xx}, \tau_{xy}, \tau_{yy}) \equiv (\tau_i)$, assume the form

$$\tau_i = a_i x^{c_i+d_i} y^{c_i} + b_i, \tag{43}$$

where

$$\begin{aligned} b_1 &= -\frac{2\mu_e}{\mu(2\,We - 1)}, & d_1 &= 2 - \frac{1}{We}, \\ b_2 &= 0, & d_2 &= -\frac{1}{We}, \\ b_3 &= -\frac{2\mu_e}{\mu(2\,We + 1)}, & d_3 &= -2 - \frac{1}{We}, \end{aligned} \tag{44}$$

for $We < 1/2$. This is a condition that emerges on the normal stress component, similar to that observed in steady uniaxial extension. The pressure can now be obtained by substitution of the velocity field (satisfying the incompressibility constraint) and the stress, specified by Eqs. (43) and (44), into the balance of momentum. In order for the pressure to be compatible (satisfying commutativity with respect to differential operators), the following restrictions hold between the coefficients a_i and c_i,

$$\begin{aligned} a_1 &= -\frac{a_2 c_2}{c_1 + d_1}, & c_1 &= c_2 - 1, \\ a_3 &= -\frac{a_2(c_2 + d_2)}{c_3}, & c_3 &= c_2 + 1, \end{aligned} \tag{45}$$

for which the divergence of stress vanishes. For the pressure, that balances with the convection term, we then obtain

$$p = -\frac{Re}{2}(x^2 + y^2). \tag{46}$$

Only the coefficients a_2 and c_2 can be chosen freely; we take $a_2 = c_2 = 1$. On the two inflow boundaries, at $x = x_0$ and $y = y_1$, the corresponding values of τ_i are prescribed. For the non-dimensional numbers, we select $We = 0.1$, $Re = 1$, $\mu_e/\mu = 8/9$ and $\mu_s/\mu = 1/9$. Measures of accuracy are taken as above under the maximum norm.

7 Results for pure convection problem

For calibration, we concentrate on error norms that measure the departure from the analytical solution with mesh refinement under various settings. We consider both a linear integral evaluation, based on the linearised advection speed of section 4.2 with linear stress and velocity representation in the source terms, and a quadratic integral evaluation, based on quadratic velocity and stress representation obtained from the parent finite element, as discussed in section 5.

7.1 FE/SUPG method

Here, we first establish the performance characteristics for the finite element method with SUPG upwinding. The difference from the exact solution for the pure convection problem with mesh refinement, a fixed velocity field and domain 1, are displayed in Fig. 11 and Table 1. Unless otherwise stated all figures pertain to a fixed velocity field by default. Results are recorded for ϕ_2 and ϕ_3 only, as the computation for the bilinear ϕ_1 solution is exact. Fig. 11 shows almost $\mathcal{O}(h^3)$ convergence in the maximum norm for ϕ_2, as to be expected from the quadratic FE basis functions for scalar solutions ϕ. The maximum allowable non-dimensional time step for the 16x16 mesh was $\Delta t = 0.002$. To obtain convergence 698 time steps were necessary, which took 90 s of CPU-time on a Dec-alpha EV56 processor. We will take this CPU-time as a reference scale against which to compare the performance of the alternative implementations.

7.2 Comparison of flux distribution schemes

In this section, results for ϕ_2 in Fig. 11 and for ϕ_3 in Table 1 are presented on accuracy for the FV scheme variants, as described in section 4. The close tally between ϕ_2 and ϕ_3 results is evident. This includes error norms for the N-scheme (linear, positive), LDB-scheme (linear, linearity preserving) and PSI-scheme (nonlinear, linearity preserving, positive), respectively. The linearised advection velocity approach, as discussed in section 4.2, is assumed initially.

As all components ϕ_i obtain the same accuracy for the three schemes, the norms for ϕ_1 are omitted.

What is immediately clear for this model problem, is that the linearity preservation property is essential to obtain the higher levels of accuracy. The PSI- and LDB-scheme display $\mathcal{O}(h^2)$ convergence, whilst the N-scheme only achieves $\mathcal{O}(h^{0.8})$. For this reason, under the present circumstance, henceforth we may disregard the N-scheme. Furthermore, it is notable that for the N-scheme and PSI-scheme (β-schemes), two to three times as many time steps were necessary for convergence, as can be observed from Table 2. This is not caused by the inconsistent treatment for the time terms of the β-schemes, as with the LDB-scheme (an α-scheme), using the inconsistent MDC approach for the time terms did not change the number of time steps significantly. Thus, we conclude that the LDB-scheme renders the fastest convergence rate. The non-dimensional time step used for the 16x16 mesh was $\Delta t = 0.005$ for all the FV methods, which is 2.5 times the maximum allowable time step for the FE/SUPG method. For the LDB-scheme, the number of time steps required for convergence was 150. Thus, even with the difference in time step from FE/SUPG taken into account, convergence of the LDB-scheme is considerably faster. Furthermore, the CPU-time resource demanded was much lower for the LDB-scheme, being less than 2% of the time for the FE/SUPG implementation.

On the basis of this evidence, the average velocity assumption would seem reasonable. However, as we shall demonstrate, these schemes may not display $\mathcal{O}(h^2)$ accuracy for all flows. Subsequently, we restrict ourselves to the LDB-scheme, as this provides the best alternative on a performance level.

7.3 Influence of velocity parallelism to boundaries

First we consider the case of linear FV integral evaluation, taking into account a change in flow with domains 2 and 3. For domain 2, the flow in the neighbourhood of the lower boundary $y_0 = 0.1$ is *nearly parallel* to this station. Then, $\mathcal{O}(h^2)$ convergence with mesh refinement may be lost for the linear integral evaluation, as may be discerned from the error norm for ϕ_1 in Fig. 12. For ϕ_1, as well as for the omitted ϕ_2 and ϕ_3, only approximately $\mathcal{O}(h^{1.4})$ is obtained.

For domain 3, the flow at the lower boundary $y_0 = 0$ is *parallel* to that location. Fig. 12 shows, that in this case, the solution for ϕ_1 becomes more inaccurate with the linear integral evaluation. In fact, for the bilinear case ϕ_1 the anomalous result of $\mathcal{O}(h)$ convergence is observed, contrary to that of $\mathcal{O}(h^2)$ as anticipated. This result corresponds to the accuracy of standard upwinding methods. This is clearly the more severe scenario, as ϕ_2 displays $\mathcal{O}(h^{1.5})$ and ϕ_3 the anticipated $\mathcal{O}(h^2)$ accuracy. The accuracy for ϕ_2 is optimal, as the second derivative with respect to y is proportional to $y^{-1/2}$, which indicates why $\mathcal{O}(h^{1.5})$ convergence prevails.

In Fig. 13 the point of attention shifts to comparison between the linear and quadratic FV integral evaluations, displaying the increased accuracy for domain 2 when the quadratic option is invoked. The results prove to be exact for the bilinear case ϕ_1 and are hence not shown. For the remaining ϕ_i, we observe that $\mathcal{O}(h^2)$ convergence is recovered once again.

For domain 3, once more, the optimal position of exact results is recovered for the bilinear case (not shown). The two remaining components show the same optimal accuracy as the linear evaluation of the integrals. For the quadratic ϕ_3 component, we observe $\mathcal{O}(h^2)$ convergence, whilst the optimal order for ϕ_2 of $\mathcal{O}(h^{1.5})$ is attained (due to the singularity in the second derivative at $y = 0$, as discussed above; optimality of order may be gathered

from a Taylor series expansion of the solution). Therefore, we conclude that, for the velocity parallel to boundaries, the linear integral evaluation does not yield results of comparable quality to that developed for domain 1 flow. Here we have successfully demonstrated that by including a more accurate representation of velocity and stress on the element boundaries, this deficiency may be overridden. Whether this is due to the improved accuracy in the stress or velocity remains to be established.

For the more accurate integral evaluation, the price is a degradation in efficiency: 0.14 compared to 0.02 time units for the linear evaluation, though as yet the implementation with quadratic evaluation has not been fully optimised. However, the increased efficiency compared to FE/SUPG is manifest. The number of time steps, maximum allowable time step and relative CPU-time for the various distribution schemes and integral evaluation methods are summarised in Table 2.

8 Results for Oldroyd-B flow problem

For this problem, we demonstrate the influence of the inclusion of source terms alongside the fluxes. We follow the pattern above and first provide the performance characteristics for the benchmark FE/SUPG method.

8.1 FE/SUPG method

The results for the finite element method with SUPG upwinding and fixed velocity field are presented in Fig. 14 for domain 1. We note the accuracy for the coarser meshes is between $\mathcal{O}(h)$ and $\mathcal{O}(h^2)$ for the various stress components, and that this increases with increasing mesh refinement, to between $\mathcal{O}(h^{2.2})$ and $\mathcal{O}(h^{2.7})$. The averaged estimates of slopes are $\mathcal{O}(h^{2.4})$, $\mathcal{O}(h^2)$ and $\mathcal{O}(h^{1.6})$ for τ_{xx}, τ_{xy} and τ_{yy}, respectively. These are noted to have reduced from the cubic order (constant slope) of the pure convection problem, that is without source terms. However, for the Oldroyd problem and finer meshes, the trend is improving towards cubic behaviour. The maximum allowable time step on the most refined 16x16 mesh was $\Delta t = 0.002$. Some 627 time steps were required for convergence, which equates to 1.2 time units.

8.2 Influence of velocity parallelism to boundaries

In Fig. 14 and Table 3 we compare the FV method employing linear integral evaluation with FE/SUPG. This demonstrates that when sources are treated consistently in the FV scheme, almost second-order accuracy is obtained on domain 1 for all stress components. It is conspicuous that τ_{xy} is more accurately represented by the FV than the FE scheme. For the linear integral evaluation, Fig. 15 and Table 4 show the loss of accuracy across all components for domain 2, where the velocity at the lower boundary is almost parallel to it. In this case, we observe $\mathcal{O}(h)$ convergence for both τ_{xx} and τ_{xy}, whilst for τ_{yy} we have approximately $\mathcal{O}(h^{1.4})$. Furthermore, we detect from Fig. 15 that, in contrast to the above, we obtain the desired $\mathcal{O}(h^2)$ convergence with the quadratic integral evaluation in all stress components.

We conclude with the important result, that introducing source terms in a consistent manner, does not detract from the accuracy of the FV scheme. The same shortcomings, concerning the loss of accuracy when the velocity is almost parallel to a boundary, are observed as for the pure convection problem: these may be overcome in a likewise fashion. The reason for this degradation in accuracy may be attributed to the observation that, on the boundary, the nodes mainly receive contributions from only one FV-cell. This suggests

the phenomenon is local to the boundary. If this is the case, then the special treatment with quadratic FV integral evaluation can be confined to boundary points only. This is an issue that is consigned to further research.

8.3 Hybrid FE/FV method

In this section, we include the solution of the pressure and velocity by the FE pressure-correction method of section 3, to demonstrate the effective coupling of the FE and FV components of the hybrid scheme.

The corresponding results on accuracy for the stress are displayed in Fig. 16. There, the stress for the hybrid scheme is compared with the case of fixed velocity, which is referred to as the uncoupled case. For completeness, the accuracy results of the hybrid scheme for velocity and pressure are shown in Fig. 17.

For all variables the accuracy attained is between $\mathcal{O}(h^2)$ and $\mathcal{O}(h^3)$. The velocities and τ_{xx} reflect almost $\mathcal{O}(h^3)$ accuracy, whilst for τ_{xy} and τ_{yy} the accuracy is somewhat more than $\mathcal{O}(h^2)$. There is an improvement in order of accuracy from the uncoupled to hybrid cases, but this may be attributed to slightly more inaccurate solutions calculated on the coarser meshes, see Fig. 16. For the pressure we observe $\mathcal{O}(h^{2.6})$.

We conclude that, the anticipated third and second-order accuracy for velocity and pressure from FE discretisation, respectively, is not influenced detrimentally under the hybrid FE/FV scheme. For the stress, a loss of one order of accuracy is anticipated by shifting from the quadratic finite element to the four finite volume subcells. Compared to the uncoupled case, the accuracy on the coarser meshes is somewhat lower for the hybrid scheme. For the finer meshes, however, comparable accuracy levels are achieved.

The gains are in terms of efficiency. The efficiency of the hybrid scheme is dominated by the momentum and pressure-correction stage, which takes approximately the same CPU-time as does the FE/SUPG for stress. As the FV implementation for stress alone takes 10% of the time for the FE alternative, overall this is negligible compared to the Navier–Stokes solver solution time. Hence, a considerable gain in efficiency can be obtained with this hybrid FE/FV scheme for large problems, involving either multi-mode or three-dimensional calculations.

9 Conclusions

We have employed two model problems on various flow domains to establish the accuracy of a proposed hybrid FE/FV scheme that is capable of producing second-order accurate and efficient solutions to viscoelastic flows. We have been able to demonstrate that a cell-vertex FV method with flux distribution, based on subcells of the parent FE triangular mesh, can accommodate various types of flow specifications and source terms, when treated in a consistent manner. It has been possible to draw distinction between flows with velocities parallel to boundaries and those without, the former proving a useful and stringent test on accuracy. This has led to the advent of a superior hybrid implementation, with FV integral evaluation based on quadratic FE functions. We have also drawn out the merits of positivity and linearity preservation properties for three flux distribution schemes. Linearity preservation is found to be critical to achieving second-order accuracy; this is true for both linear and nonlinear schemes. Positivity is found to lead to slower convergence rates to steady solutions, and also does not aid accuracy. This is a property that may well impinge on stability. Attention to nonlinear stability and reaching high Weissenberg number solutions are further issues to address in a subsequent study, where it is anticipated that nonlinear

FD schemes with positivity may well prove beneficial.

No loss of accuracy for velocity and pressure is observed in the hybrid FE/FV compared to the FE/SUPG scheme. There is no loss of accuracy in the FV method between uncoupled and hybrid implementations. Also there is less than one order difference in accuracy of stress between hybrid FE/FV compared to the FE/SUPG scheme. Compared to the FE/SUPG method the hybrid FE/FV requires smaller time steps, less iterations and less CPU time per iteration. This offers the possibility of considerable gains in efficiency with this hybrid FE/FV scheme for large problems, particularly where either multi-mode or three-dimensional calculations are involved.

10 Acknowledgements

The financial support of EPSRC ROPA grant GR/K63801 and EU/TMR Network grant FMRX-CT98-0210 is gratefully acknowledged. In addition, the authors would like to thank our joint investigators on this project, Professor Peter Townsend and Dr Rhys Gwynllyw for their contributions, and Mrs Yafang Liu for assistance in the final drafting of some of the results.

References

[1] E.O.A. Carew, P. Townsend, and M.F. Webster. A Taylor–Petrov–Galerkin algorithm for viscoelastic flow. *J. Non-Newtonian Fluid Mech.*, 50:253–287, 1993.

[2] A. Baloch, P. Townsend, and M.F. Webster. On the simulation of highly elastic complex flows. *J. Non-Newtonian Fluid Mech.*, 59(2/3):111–128, 1995.

[3] H. Matallah, P. Townsend, and M.F. Webster. Recovery and stress-splitting schemes for viscoelastic flows. *J. Non-Newtonian Fluid Mech.*, 75:139–166, 1998.

[4] K.W. Morton and M.F. Paisley. A finite volume scheme with shock fitting for the steady Euler equations. *J. Comput. Phys.*, 80:168–203, 1989.

[5] P.I. Crumpton, J.A. Mackenzie, and K.W. Morton. Cell vertex algorithms for the compressible Navier–Stokes equations. *J. Comput. Phys.*, 109:1–15, 1993.

[6] R. Struijs, H. Deconinck, and P.L. Roe. Fluctuation splitting for the 2D Euler equations. Technical Report Lecture series 1990-01, Von Karman Institute for Fluid Dynamics, 1991.

[7] G.T. Tomaich and P.L. Roe. Compact schemes for advection-diffusion problems on unstructured grids. *Modelling and Simulation*, 23:2629, 1993.

[8] J.M. Marchal and M.J. Crochet. A new mixed finite element for calculating viscoelastic flow. *J. Non-Newtonian Fluid Mech.*, 26:77–114, 1987.

[9] M. Berzins and J.M. Ware. Positive cell-centred finite volume discretisation methods for hyperbolic equations on irregular meshes. *Appl. Num. Math.*, 16:417–438, 1995.

[10] C. Hirsch. *Numerical computation of internal and external flows*, volume 1. John Wiley, New York, 1988.

[11] D. Rajagopalan, R.C. Armstrong, and R.A. Brown. Finite element methods for calculation of steady, viscoelastic flow using constitutive equations with a Newtonian viscosity. *J. Non-Newtonian Fluid Mech.*, 36:159–192, 1990.

[12] F.P.T. Baaijens. Numerical analysis of unsteady viscoelastic flow. *Comp. Meth. Appl. Mech. Eng.*, 94:285–299, 1992.

[13] R. Guénette and M. Fortin. A new mixed finite element method for computing viscoelastic flows. *J. Non-Newtonian Fluid Mech.*, 60:27–52, 1995.

[14] F.P.T. Baaijens. An iterative solver for the DEVSS/DG method with application to smooth and non-smooth flows of the upper convected Maxwell fluid. *J. Non-Newtonian Fluid Mech.*, 75:119–138, 1998.

[15] A. Baloch, P. Townsend, and M.F. Webster. On vortex development in viscoelastic expansion and contraction flows. *J. Non-Newtonian Fluid Mech.*, 65:133–149, 1996.

[16] S.-C. Xue, N. Phan-Thien, and R.I. Tanner. Three dimensional numerical simulations of viscoelastic flows through planar contractions. *J. Non-Newtonian Fluid Mech.*, 74:195–245, 1998.

[17] C. Béraudo, A. Fortin, T. Coupez, Y. Demay, B. Vergnes, and J.F. Agassant. A finite element method for computing the flow of multi-mode viscoelastic fluids: comparison with experiments. *J. Non-Newtonian Fluid Mech.*, 75:1–23, 1998.

[18] C.D. Eggleton, T.H. Pulliam, and J.H. Ferziger. Numerical simulation of viscoelastic flow using flux difference splitting at moderate Reynolds numbers. *J. Non-Newtonian Fluid Mech.*, 64:269–298, 1996.

[19] M.S. Darwish, J.R. Whiteman, and M.J. Bevis. Numerical modelling of viscoelastic liquids using a finite volume method. *J. Non-Newtonian Fluid Mech.*, 45:311–337, 1992.

[20] S.-C. Xue, N. Phan-Thien, and R.I. Tanner. Numerical study of secondary flows of viscoelastic fluid in straight pipes by an implicit finite volume method. *J. Non-Newtonian Fluid Mech.*, 59:191–213, 1995.

[21] X. Huang, N. Phan-Thien, and R.I. Tanner. Viscoelastic flow between eccentric rotating cylinders: unstructured control volume method. *J. Non-Newtonian Fluid Mech.*, 64:71–92, 1996.

[22] T. Sato and S.M. Richardson. Explicit numerical simulation of time-dependent viscoelastic flow problems by a finite-element/finite-volume method. *J. Non-Newtonian Fluid Mech.*, 51:249–275, 1994.

[23] J.Y. Yoo and Y. Na. A numerical study of the planar contraction flow of a viscoelastic fluid using the SIMPLER algorithm. *J. Non-Newtonian Fluid Mech.*, 39:89–106, 1991.

[24] G. Mompean and M. Deville. Unsteady finite volume simulation of Oldroyd-B fluid through a three-dimensional planar contraction. *J. Non-Newtonian Fluid Mech.*, 72:253–279, 1997.

[25] S. Gunter, P. Townsend, and M.F. Webster. The simulation of some model viscoelastic extensional flows. *Int. J. Num. Methods Fluids*, 23:691–710, 1996.

[26] R.B. Bird, R.C. Armstrong, and O. Hassager. *Dynamics of polymeric liquids*, volume 1. John Wiley, New York, 2nd edition, 1987.

[27] P. Townsend and M.F. Webster. An algorithm for the three-dimensional transient simulation of non-Newtonian fluid flows. In G.N. Pande and J. Middleton, editors, *Transient/dynamic analysis and constitutive laws for engineering materials, Int. Conf. Numerical Methods in Engineering: Theory and Applications - NUMETA 87*, volume 2, pages T12/1–11. Kluwer Academic Publishers, Dordrecht, 1987.

[28] D.M. Hawken, P. Townsend, and M.F. Webster. A Taylor–Galerkin-based algorithm for viscous incompressible flow. *Int. J. Num. Methods Fluids*, 10:327–351, 1990.

[29] M.E. Hubbard. A survey of genuinely multidimensional upwinding techniques. Technical Report Numerical Analysis Report 7/93, University of Reading, 1993.

Table legend

Table 1: Error norm behaviour $||\Delta\phi_3||_\infty$ for pure convection problem; comparison of various FV schemes against FE/SUPG, domain 1.

Table 2: Number of time steps n, maximum time step and CPU time relative to FE/SUPG; comparison of schemes and FV integral evaluation, pure convection problem, domain 1, mesh 16x16.

Table 3: Infinity norm error behaviour of stress for Oldroyd-B problem; comparison between FE/SUPG and LDB-scheme, domain 1, fixed velocity, linear FV integral evaluation.

Table 4: Infinity norm error behaviour of stress for Oldroyd-B problem; comparison between integral evaluation approaches, domain 2, LDB-scheme, fixed velocity.

Figure legend

Figure 1: Triangular cell with one inflow side.

Figure 2: Triangular cell with two inflow sides.

Figure 3: Graphical representation of LDB-scheme defining γ_1 and γ_2.

Figure 4: Schematic diagram of finite element/finite volume triangular mesh.

Figure 5: Triangular finite volume grid with median dual cell (MDC) for node i.

Figure 6: Finite volume node 1 at a corner with surrounding FV-cells and median dual cell sections A, B.

Figure 7: Structured 2x2 finite element mesh with minimum and maximum coordinates.

Figure 8: Velocity vectors for pure convection and Oldroyd-B flow problem, domain 1.

Figure 9: Isolines for pure convection problem, ϕ_2, domain 1.

Figure 10: Contour lines of stress and pressure for Oldroyd-B flow problem, domain 1: a) τ_{xx}, b) τ_{xy}, c) τ_{yy}, d) p.

Figure 11: Error norm behaviour $||\Delta\phi_2||_\infty$ for pure convection problem; comparison of various FV schemes against FE/SUPG, linear FV integral evaluation, domain 1.

Figure 12: Error norm behaviour $||\Delta\phi_1||_\infty$ for pure convection problem; comparison across various domains, LDB-scheme, linear FV integral evaluation.

Figure 13: Error norm behaviour $||\Delta\phi_2||_\infty$ and $||\Delta\phi_3||_\infty$ for pure convection problem; comparison between FV integral evaluation, domain 2, LDB-scheme.

Figure 14: Infinity norm error behaviour of stress for Oldroyd-B problem; comparison between FE/SUPG and LDB-scheme, domain 1, fixed velocity, linear FV integral evaluation.

Figure 15: Infinity norm error behaviour of stress for Oldroyd-B problem; comparison between integral evaluation approaches, domain 2, LDB-scheme, fixed velocity.

Figure 16: Infinity norm error behaviour of stress for Oldroyd-B problem; comparison between uncoupled and hybrid method, domain 2, LDB-scheme, quadratic FV integral evaluation.

Figure 17: Infinity norm error behaviour of pressure and velocity for Oldroyd-B problem; domain 2, LDB-scheme, quadratic FV integral evaluation.

Table 1: Error norm behaviour $||\Delta\phi_3||_\infty$ for pure convection problem; comparison of various FV schemes against FE/SUPG, domain 1.

	FE	FV		
	SUPG	N	LDB	PSI
2x2	$0.20\,10^{-2}$	$0.19\,10^{-1}$	$0.19\,10^{-2}$	$0.24\,10^{-2}$
4x4	$0.28\,10^{-3}$	$0.12\,10^{-1}$	$0.48\,10^{-3}$	$0.52\,10^{-3}$
8x8	$0.38\,10^{-4}$	$0.64\,10^{-2}$	$0.12\,10^{-3}$	$0.14\,10^{-3}$
16x16	$0.50\,10^{-5}$	$0.34\,10^{-2}$	$0.12\,10^{-3}$	$0.35\,10^{-4}$

Table 2: Number of time steps n, maximum time step and CPU time relative to FE/SUPG; comparison of schemes and FV integral evaluation, pure convection problem, domain 1, mesh 16x16.

	n	Δt	CPU (units)
FE/SUPG	698	0.002	1.00
N	359	0.005	0.03
LDB (linear)	150	0.005	0.02
LDB (quadratic)	165	0.005	0.14
PSI	395	0.005	0.04

Table 3: Infinity norm error behaviour of stress for Oldroyd-B problem; comparison between FE/SUPG and LDB-scheme, domain 1, fixed velocity, linear FV integral evaluation.

	FE/SUPG			FV/LDB		
	$\|\|\tau_{xx}\|\|_\infty$	$\|\|\tau_{xy}\|\|_\infty$	$\|\|\tau_{yy}\|\|_\infty$	$\|\|\tau_{xx}\|\|_\infty$	$\|\|\tau_{xy}\|\|_\infty$	$\|\|\tau_{yy}\|\|_\infty$
2x2	$0.10\,10^{-2}$	$0.24\,10^{-2}$	$0.59\,10^{-2}$	$0.79\,10^{-3}$	$0.18\,10^{-2}$	$0.14\,10^{-1}$
4x4	$0.26\,10^{-3}$	$0.74\,10^{-3}$	$0.28\,10^{-2}$	$0.27\,10^{-3}$	$0.41\,10^{-3}$	$0.45\,10^{-2}$
8x8	$0.47\,10^{-4}$	$0.19\,10^{-3}$	$0.92\,10^{-3}$	$0.86\,10^{-4}$	$0.10\,10^{-3}$	$0.12\,10^{-2}$
16x16	$0.72\,10^{-5}$	$0.37\,10^{-4}$	$0.20\,10^{-3}$	$0.25\,10^{-4}$	$0.25\,10^{-4}$	$0.33\,10^{-3}$

Table 4: Infinity norm error behaviour of stress for Oldroyd-B problem; comparison between integral evaluation approaches, domain 2, LDB-scheme, fixed velocity.

	linear integral evaluation			quadratic integral evaluation		
	$\|\|\tau_{xx}\|\|_\infty$	$\|\|\tau_{xy}\|\|_\infty$	$\|\|\tau_{yy}\|\|_\infty$	$\|\|\tau_{xx}\|\|_\infty$	$\|\|\tau_{xy}\|\|_\infty$	$\|\|\tau_{yy}\|\|_\infty$
2x2	$0.22\,10^{-2}$	$0.28\,10^{-2}$	$0.34\,10^{-2}$	$0.73\,10^{-3}$	$0.27\,10^{-2}$	$0.38\,10^{-2}$
4x4	$0.12\,10^{-2}$	$0.16\,10^{-2}$	$0.10\,10^{-2}$	$0.19\,10^{-3}$	$0.73\,10^{-3}$	$0.99\,10^{-3}$
8x8	$0.54\,10^{-3}$	$0.79\,10^{-3}$	$0.44\,10^{-3}$	$0.36\,10^{-4}$	$0.18\,10^{-3}$	$0.21\,10^{-3}$
16x16	$0.23\,10^{-3}$	$0.35\,10^{-3}$	$0.18\,10^{-3}$	$0.57\,10^{-5}$	$0.43\,10^{-4}$	$0.40\,10^{-4}$

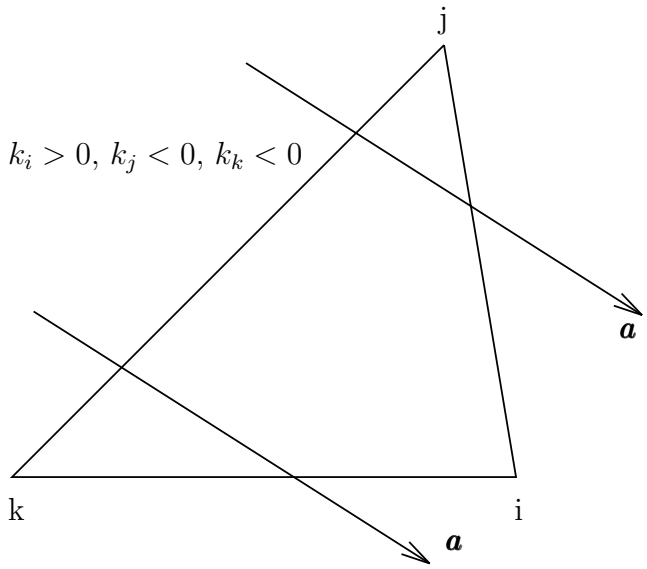

Figure 1: Triangular cell with one inflow side.

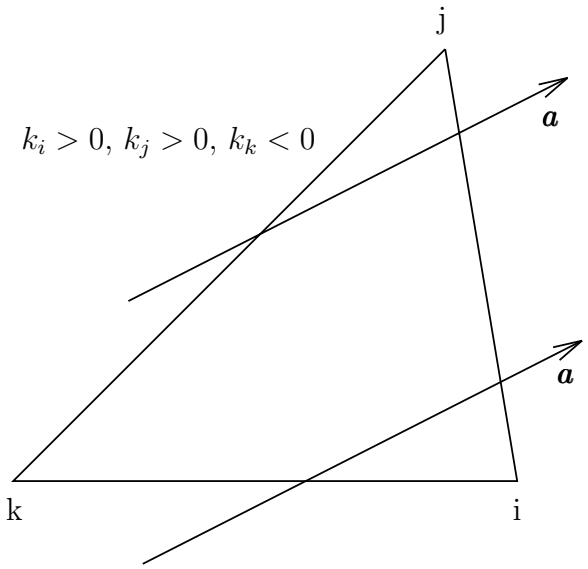

Figure 2: Triangular cell with two inflow sides.

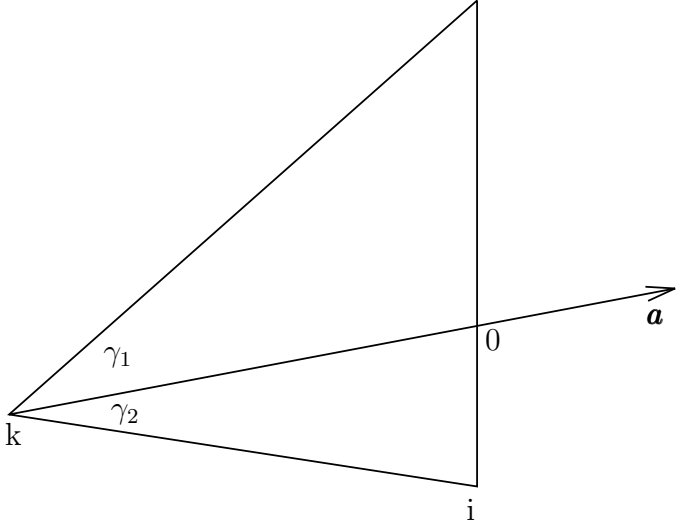

Figure 3: Graphical representation of LDB-scheme defining γ_1 and γ_2.

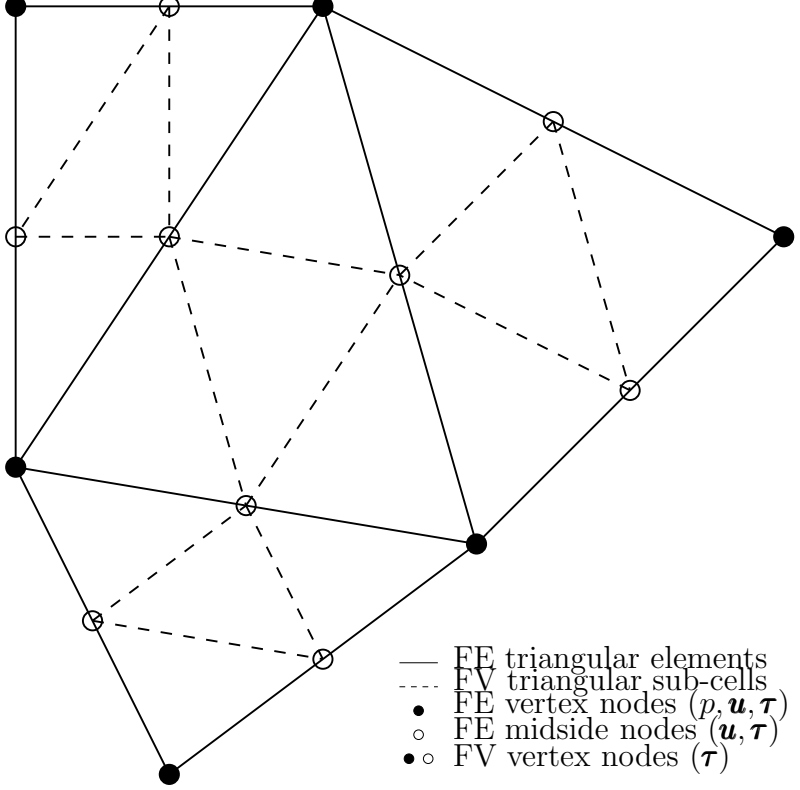

Figure 4: Schematic diagram of finite element/finite volume triangular mesh.

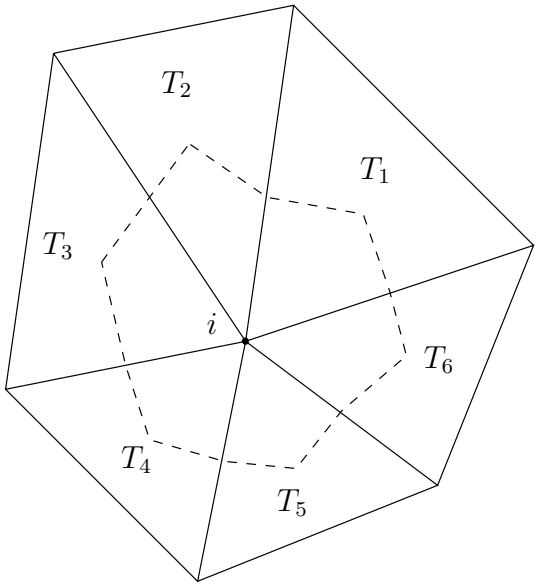

Figure 5: Triangular finite volume grid with median dual cell (MDC) for node i.

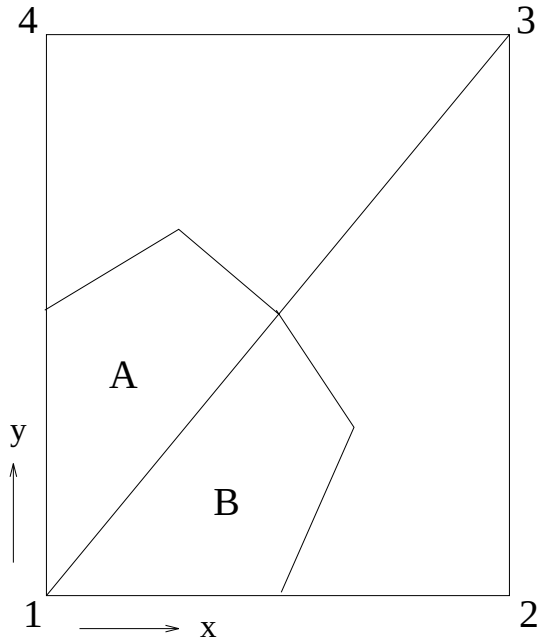

Figure 6: Finite volume node 1 at a corner with surrounding FV-cells and median dual cell sections A, B.

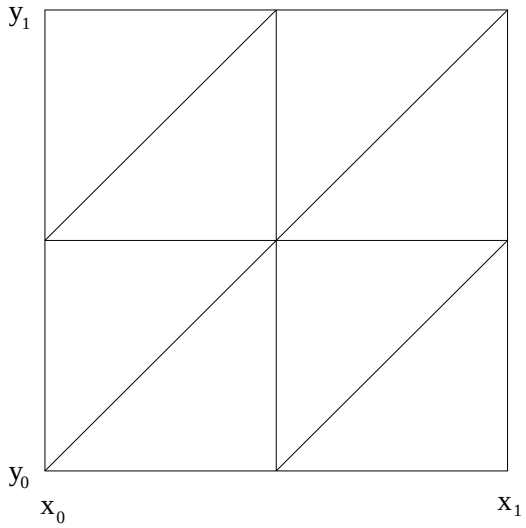

Figure 7: Structured 2x2 finite element mesh with minimum and maximum coordinates.

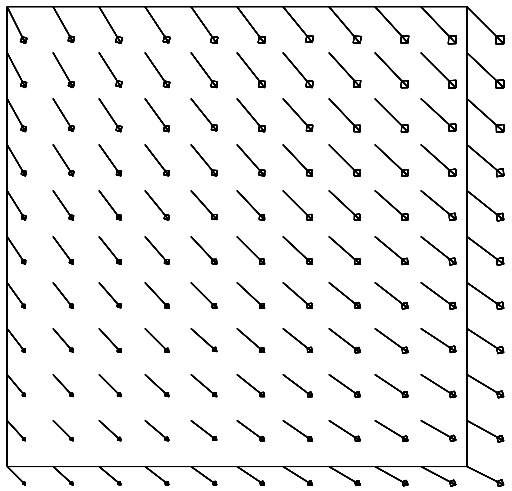

Figure 8: Velocity vectors for pure convection and Oldroyd-B flow problem, domain 1.

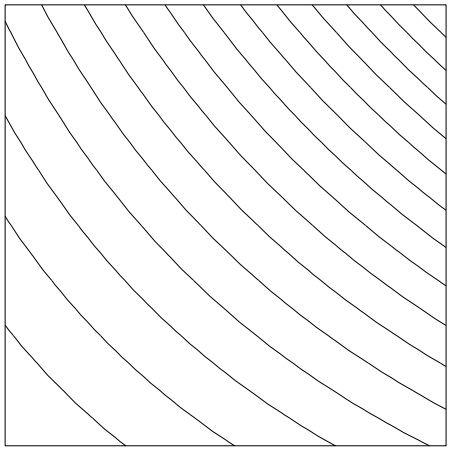

Figure 9: Isolines for pure convection problem, ϕ_2, domain 1.

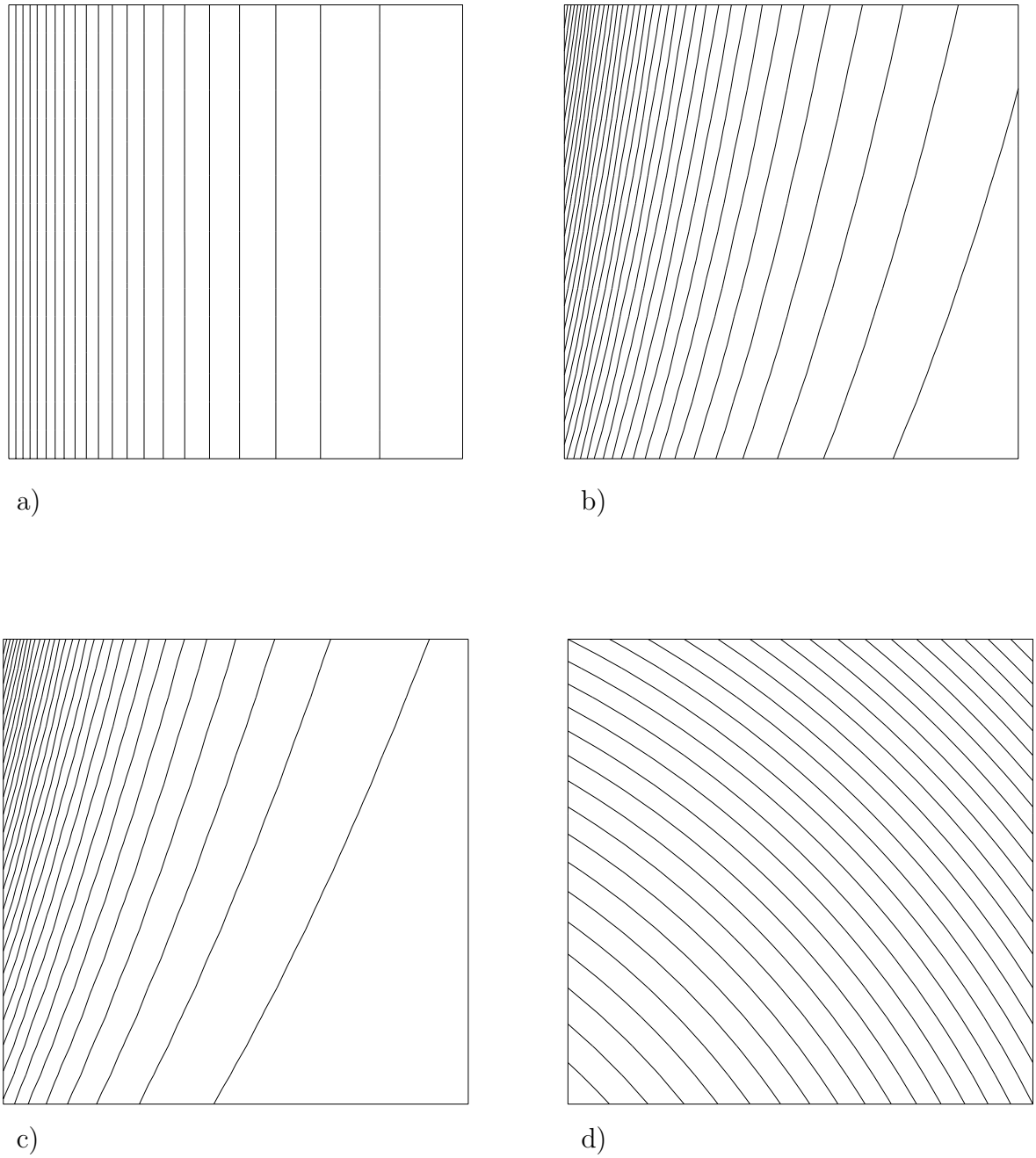

Figure 10: Contour lines of stress and pressure for Oldroyd-B flow problem, domain 1: a) τ_{xx}, b) τ_{xy}, c) τ_{yy}, d) p.

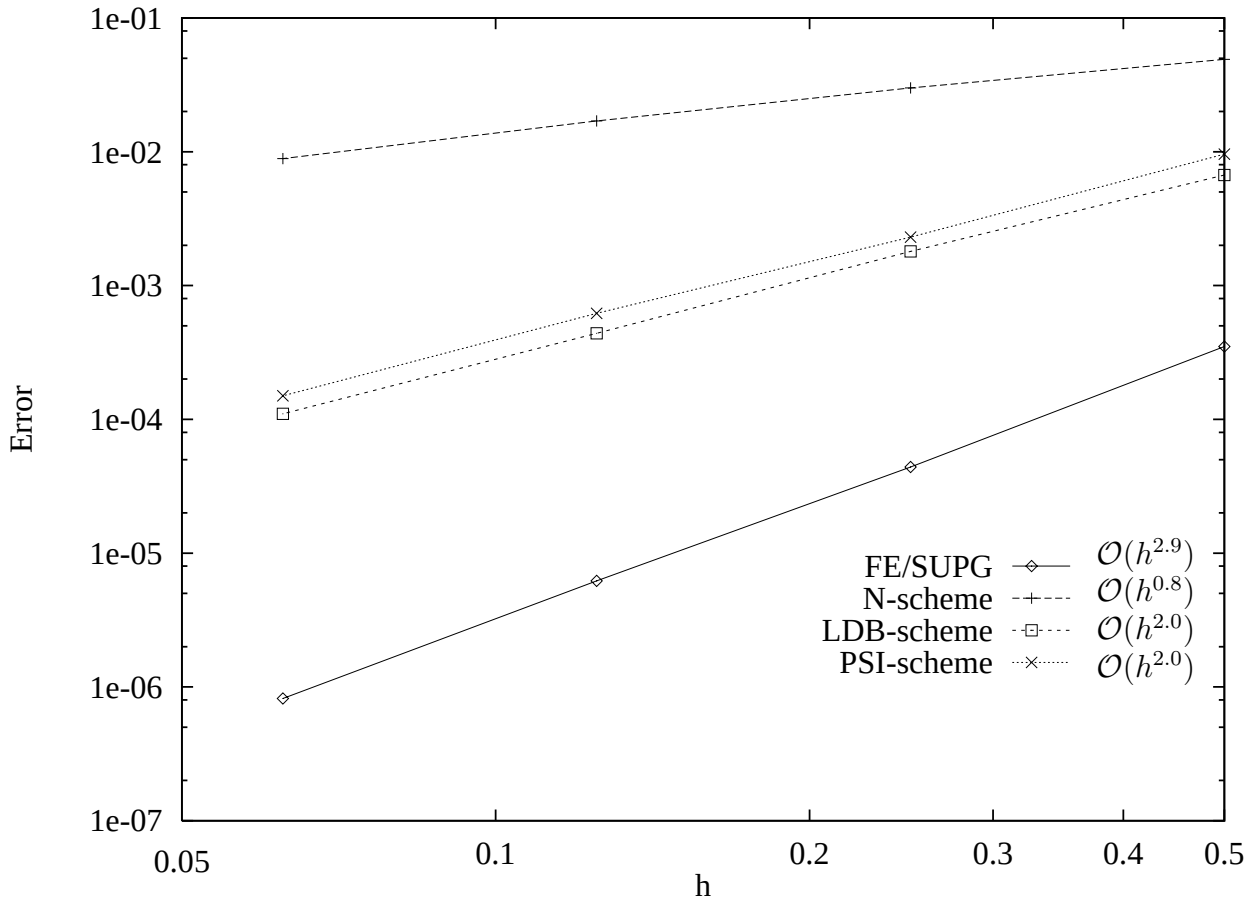

Figure 11: Error norm behaviour $||\Delta\phi_2||_\infty$ for pure convection problem; comparison of various FV schemes against FE/SUPG, linear FV integral evaluation, domain 1.

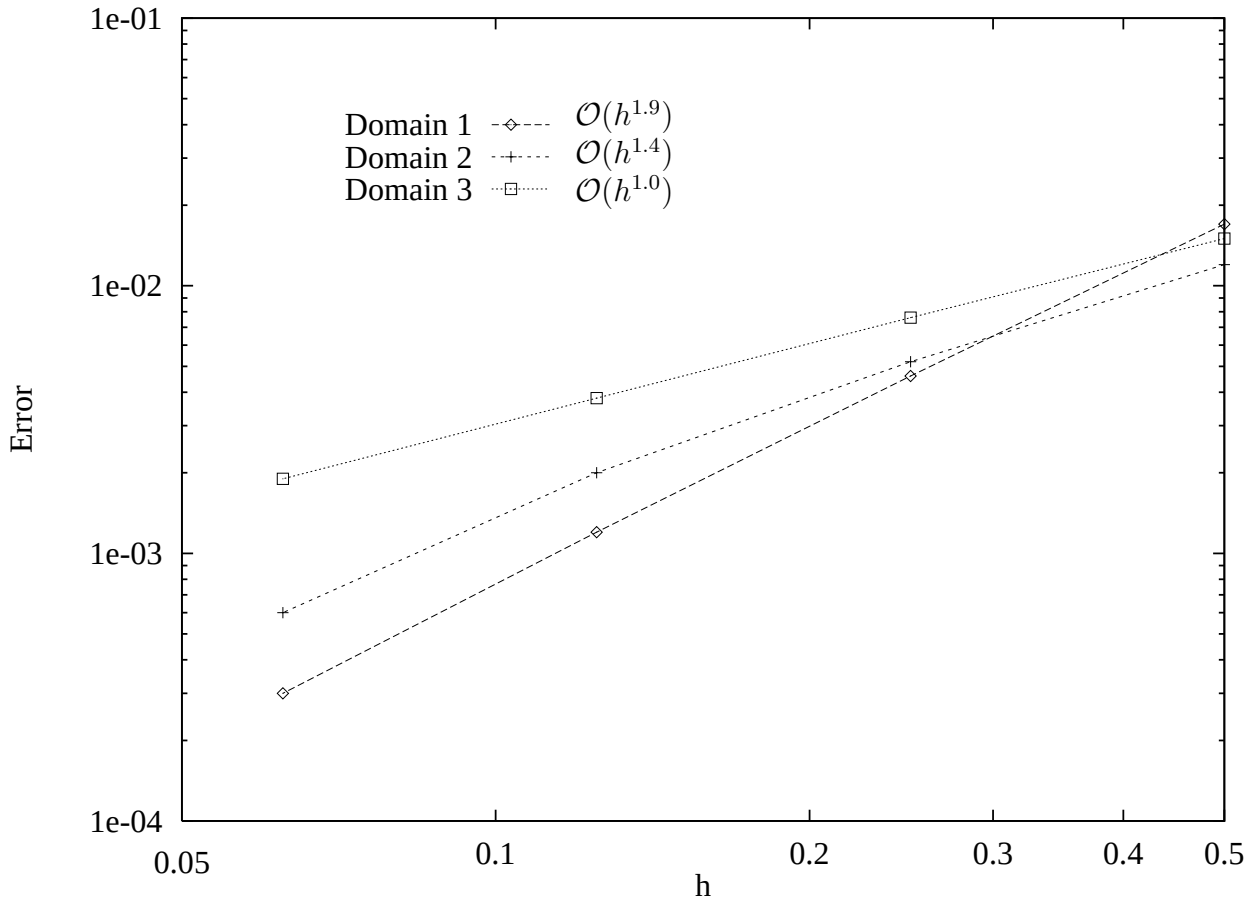

Figure 12: Error norm behaviour $||\Delta\phi_1||_\infty$ for pure convection problem; comparison across various domains, LDB-scheme, linear FV integral evaluation.

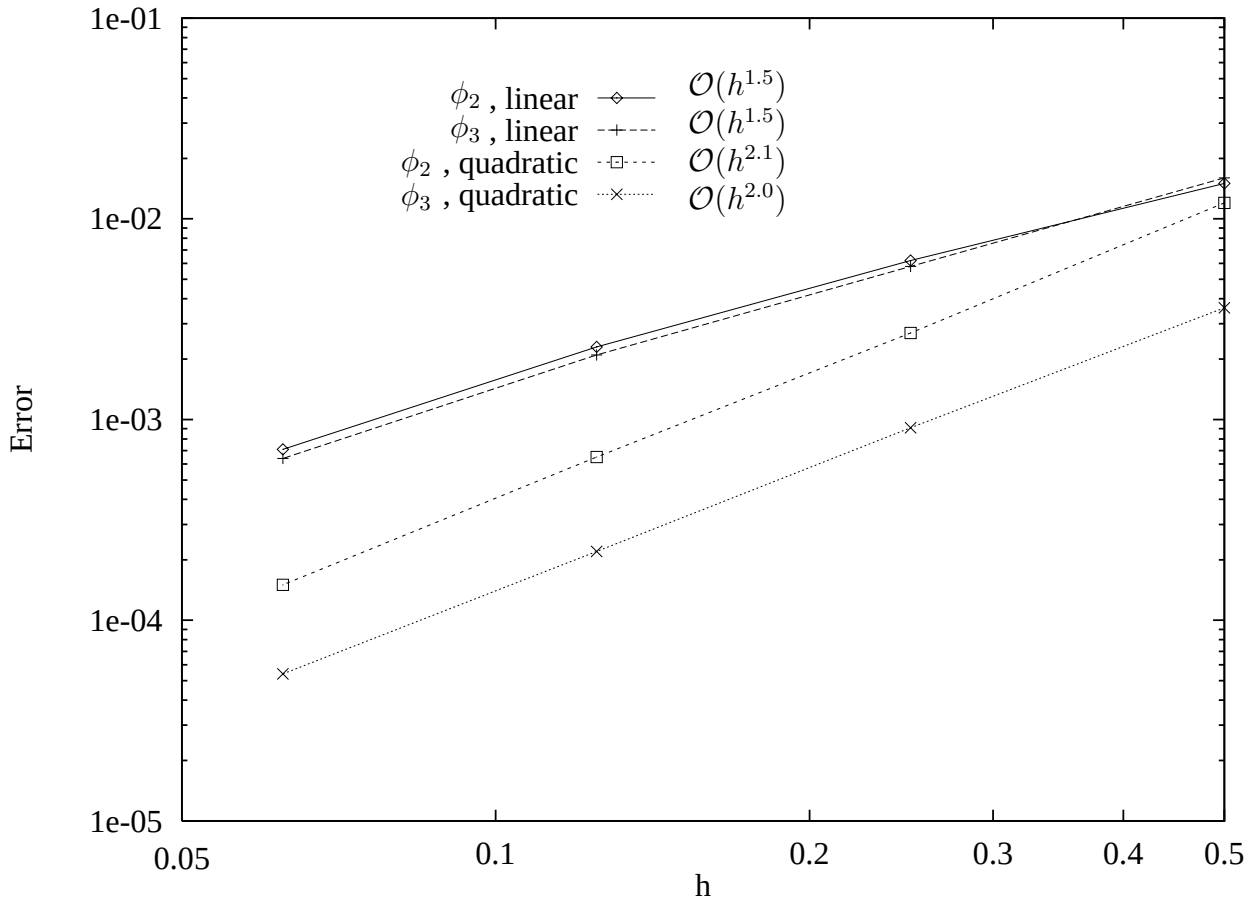

Figure 13: Error norm behaviour $||\Delta\phi_2||_\infty$ and $||\Delta\phi_3||_\infty$ for pure convection problem; comparison between FV integral evaluation, domain 2, LDB-scheme.

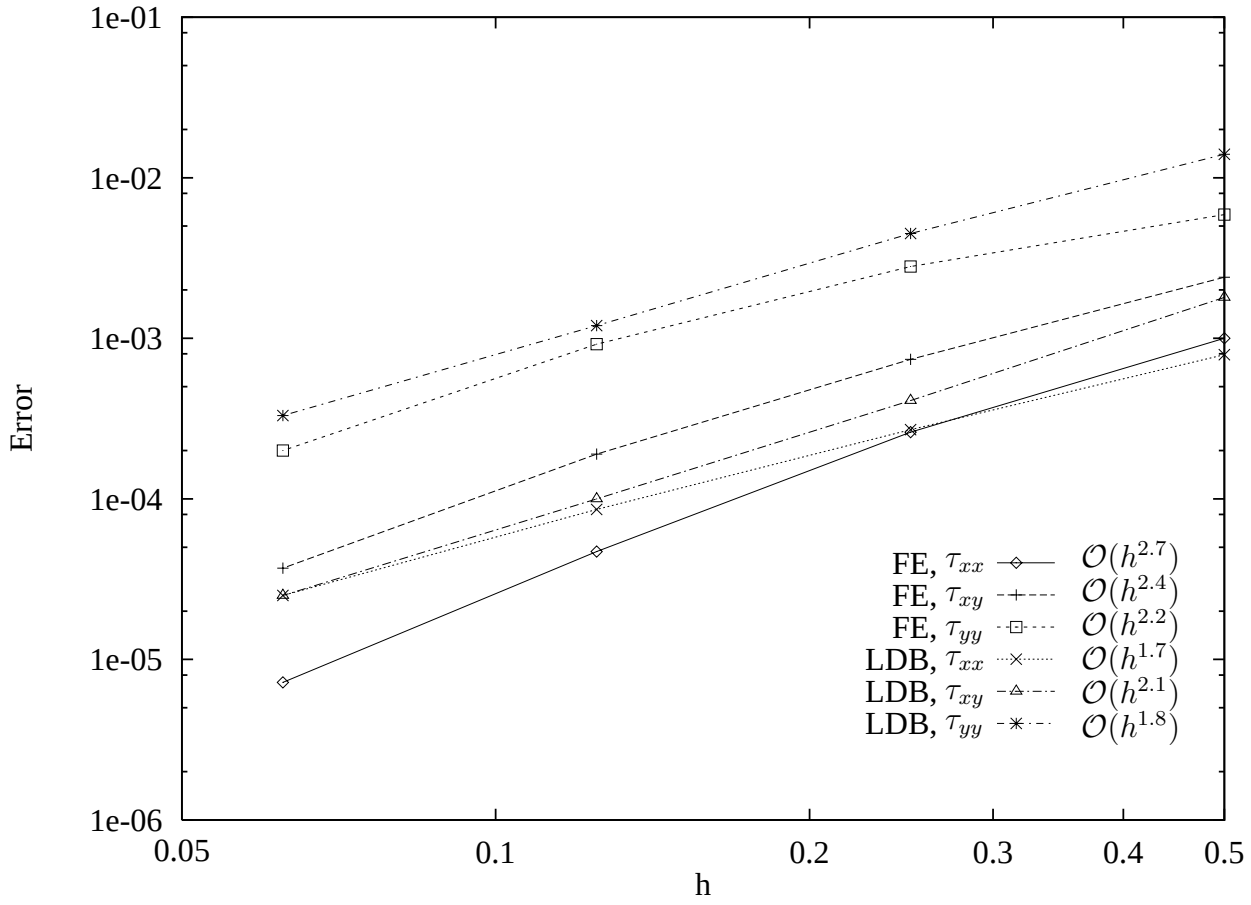

Figure 14: Infinity norm error behaviour of stress for Oldroyd-B problem; comparison between FE/SUPG and LDB-scheme, domain 1, fixed velocity, linear FV integral evaluation.

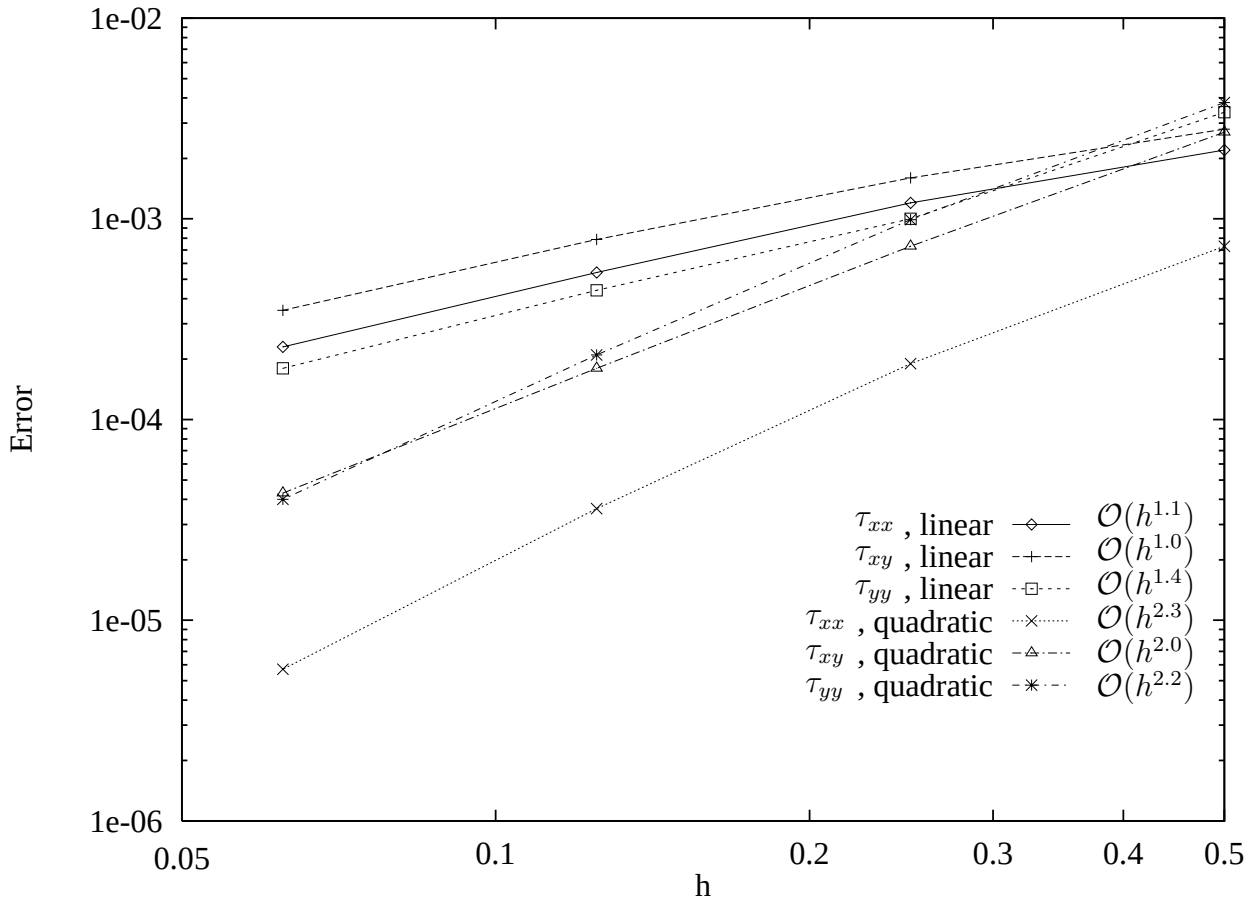

Figure 15: Infinity norm error behaviour of stress for Oldroyd-B problem; comparison between integral evaluation approaches, domain 2, LDB-scheme, fixed velocity.

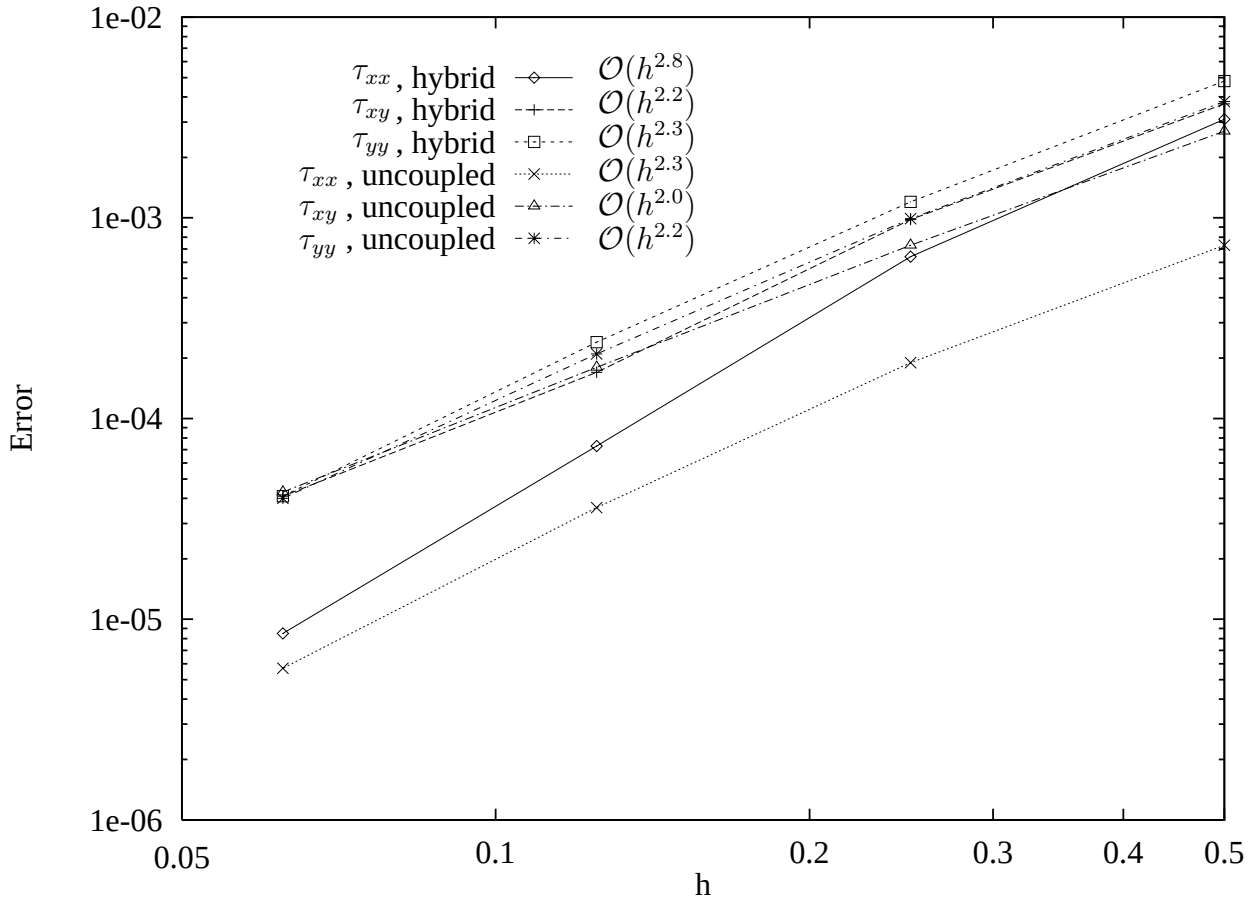

Figure 16: Infinity norm error behaviour of stress for Oldroyd-B problem; comparison between uncoupled and hybrid method, domain 2, LDB-scheme, quadratic FV integral evaluation.

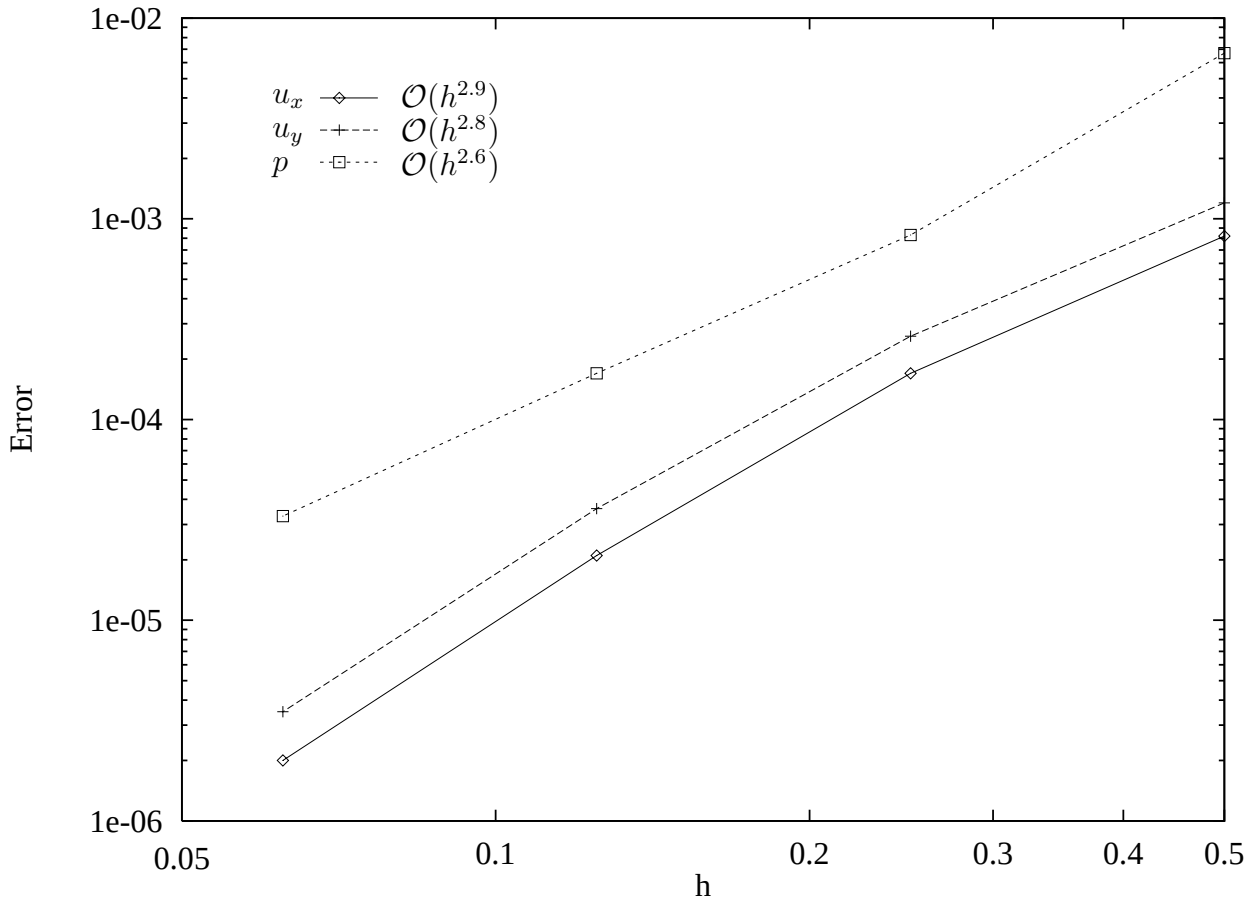

Figure 17: Infinity norm error behaviour of pressure and velocity for Oldroyd-B problem; domain 2, LDB-scheme, quadratic FV integral evaluation.